Available online at www.sciencedirect.com

SCIENCE DIRECT®

Journal of Computational Physics 187 (2003) 524–543

JOURNAL OF COMPUTATIONAL PHYSICS

www.elsevier.com/locate/jcp

Computations of bidirectional grain boundary dynamics in thin metallic films

C.M. Elliott, V. Styles *,1

Centre for Mathematical Analysis and its Applications, School of Mathematical Sciences, University of Sussex, Falmer,
Brighton BN1 9QH, UK

Received 28 March 2001; received in revised form 23 October 2002; accepted 11 November 2002

Abstract

We propose sharp interface, phase field and level set models for bidirectional diffusion induced grain boundary motion in thin films. Numerical approximations of these models are presented together with computational results comparing the approximate solutions.

PACS: 65M99; 65Z05; 74N20; 74S30

Keywords: Grain boundary motion; Computational interface evolution; Phase field; Level set

---

1. Introduction

Grain boundaries in metallic alloys arise as a result of misorientations between otherwise identical crystals. Mathematical models for the dynamics of such boundaries, in particular for diffusion induced grain boundary motion, have been studied in [3,6,9,10]. Diffusion induced grain boundary motion can be observed if a polycrystalline film of a metal is placed in a vapour containing another metal; atoms from the vapour diffuse into the film along the grain boundaries leading to variations of composition of the alloy which induces a driving force causing them to move. Solute vapour atoms are then left behind leaving alloyed regions which have been swept out by the moving grain boundary. It is believed that variations in elastic energy due to changes in composition provide a principal driving force. We refer to [11] for a material science review and [3] for a discussion of mechanisms for the driving force in the context of a phase field model.

---

[*] Corresponding author.
E-mail address: v.styles@sussex.ac.uk (V. Styles).

[1] Supported by a Leverhulme 2000 Special Research Fellowship.

0021-9991/03/$ - see front matter © 2003 Elsevier Science B.V. All rights reserved.
doi:10.1016/S0021-9991(03)00122-0

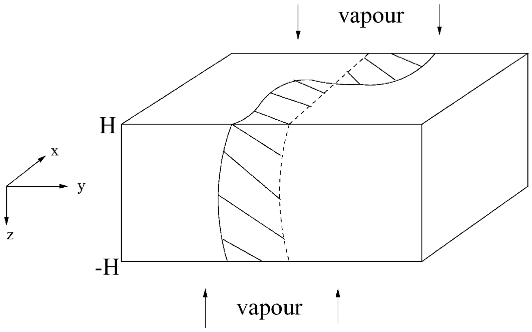

Fig. 1. Physical setup.

The physical setup we consider is a thin film of height $2H$ (H small) with vapour supplied at its top and bottom faces ($z = -H$ and $z = H$), see Fig. 1. The dashed line represents the position of a grain boundary at some initial time $t = 0$, while the solid line denotes its position after some time $t > 0$. The diffusion of solute atoms from the vapour into the film along the grain boundary creates a new region of crystalline structure behind the evolving boundary; this is the shaded region depicted in Fig. 1. Due to the thin film nature we assume independence of the z-direction and reduce the problem to a two-dimensional one for $\mathbf{x} \in \Omega := (0, L_x) \times (0, L_y)$, where Ω corresponds to the top face of the film and Γ denotes the trace of a single grain boundary (that takes the form of a simple closed curve with unit normal pointing outwards) on Ω. The setup shown in Fig. 1 of a film of uniform thickness containing a single grain boundary spanning its height and width is considered in [3] where a double obstacle phase field model for this problem is presented in which the diffuse interface is of finite thickness $\mathcal{O}(\varepsilon)$. In [9] formal asymptotics on the phase field model for $\varepsilon \to 0$ are used to obtain a sharp interface model

$$\rho V = \kappa + f(u), \tag{1.1}$$

$$\varepsilon_1 u_t = u_{ss} - Vu(1 + \varepsilon_2 \kappa), \tag{1.2}$$

where ρ is a given positive non-dimensional material constant, u denotes the concentration of solute atoms in the film, V, κ and s, respectively, denote the normal velocity, the curvature and the arc-length of the sharp interface and $\varepsilon_i = \mathcal{O}(\varepsilon)$ $i = 1, 2$. Eq. (1.1) is motion by mean curvature with a forcing dependent on concentration. Diffusion within the grain boundary is modelled by Eq. (1.2). As the grain boundary moves through the crystal it leaves a trace of vapour atoms within the crystal.

The $\mathcal{O}(\varepsilon)$ terms are in fact set to zero in [9] but are retained in [6] where independence of the y direction in Fig. 1 is assumed yielding a two-dimensional problem. The authors consider a simplified two-dimensional form of the phase field model presented in [3] together with two forms, one using a graph approach and the other a parametric approach, of the sharp interface model (1.1), (1.2). A finite element approximation of the phase field model is derived and is shown to converge to a weak solution. Also some numerical computations are presented that compare solutions of the phase field and sharp interface models. The existence of a unique weak solution to one form of the phase field system was proved in [4] while in [12] a local existence and uniqueness result for (1.1), (1.2) was obtained.

One important limitation with the theory derived in [3,9] is that only unidirectional models are allowed, such that at the outset the initial data together with reaction terms in the partial differential equations give rise to motion in a specific direction relative to the grain boundary. This limitation is eliminated in [10] where an extended sharp interface model for chemically induced grain boundary motion in the case of thin metallic films is presented. The model is that of forced mean curvature where the forcing is allowed to be ±1 or 0 on varying parts of the interface. There is no explicit concentration field. Numerical simulations are presented in [10] which illustrate the important morphological and stability effects associated with bidirectional motion. The authors solve initial value problems for nonlinear parabolic PDEs using a fourth-order Runge–Kutta method in time and central differences in space. In the following we extend the ideas presented in [10] by introducing a concentration field $u(\mathbf{x}, t)$ and an equation for its evolution and by setting the forcing term $f(u)$ in (1.1) equal to the jump in concentration across Γ. Due to the thin film nature of the setup we assume that diffusion of the solute atoms takes place very rapidly and hence we set the concentration u to equal 1 at all points of the film that Γ has passed through. This leads to the concentration field $u(\mathbf{x}, t)$ being discontinuous.

Typically for curvature dependent interface motion, see [8], there are three main numerical approaches: direct approximation of the sharp interface law, phase field and level set. In Section 2 we propose appropriate versions of these three approaches for chemically induced bidirectional grain boundary motion and in Section 3 we derive numerical approximations of these three models. We conclude with Section 4 in which we present numerical computations showing the appearance of S-shaped boundaries and double seams that are commonly observed experimentally, we also include comparisons of the approximate solutions of the three models.

2. Models

This section comprises of thin film models for chemically induced bidirectional grain boundary dynamics. We begin by introducing the free boundary model presented in [10]. Due to the thin film setup it is shown in [10] that the grain boundary Γ is almost vertical through the film and that the concentration of solute atoms u is close to 1. Thus taking $f(u) = 1$ in (1.1) and rescaling time to eliminate the factor ρ they arrive at the following free boundary problem

$$V_0 = \kappa_0 \pm 1, \tag{2.1}$$

where V_0 and κ_0, respectively, denote the normal velocity and the curvature of Γ_0, which is the intersection of Γ with the top face of the thin film. That is, in order to allow for bidirectional motion of the interface $\Gamma_0(t)$ they conceive it as being composed of two parts $\Gamma_0^+(t)$ and $\Gamma_0^-(t)$, such that Γ_0^+ is the part of the boundary that moves in the positive normal direction and Γ_0^- moves in the negative normal direction, see Fig. 2. Using (2.1) we have, after dropping the subscript '0' for simplicity of notation,

$$V = \kappa + 1 > 0 \quad \text{on } \Gamma^+(t) \tag{2.2}$$

and on $\Gamma^-(t)$

$$V = \kappa - 1 < 0 \quad \text{on } \Gamma^-(t). \tag{2.3}$$

The forcing term is taken to change discontinuously from +1 to −1 as one passes through such a transition point P. At such transition points the smoothing effect of curvature is still felt and this prevents corners occurring at such points. Observe that if the curvature is small then the two parts of the interface will move in different directions. Another situation can then occur where the grain boundaries wish to enter a region

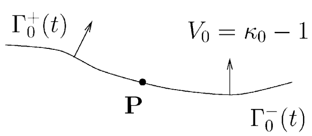

Fig. 2. Bidirectional motion.

which has already been swept out by the earlier evolution of the interface. In such a region there should be no driving force on the grain boundary.

We extend the ideas presented in [10] by explicitly introducing a concentration field and a law for its evolution. We set the forcing term $f(u)$ in (1.1) equal to the jump in concentration across Γ and set the concentration u to equal 1 at all points of the film that Γ has passed through. We suppose that the concentration u takes either the value 1 or 0 and that it jumps across curves. It follows that for a curve Γ we may set

$$[u]_\Gamma = u^+ - u^-,$$

where u^+ is the limit of u on Γ from the positive normal direction $\mathbf{v}$ and u^- is the limit on Γ from the negative normal direction $-\mathbf{v}$, see Fig. 3. We arrive at the following model:

$$V = \kappa - [u]_\Gamma, \tag{2.4}$$

$$u(\mathbf{x},t) = \begin{cases} 1 & \forall(\mathbf{x},t) \text{ such that } \mathbf{x} \in \Gamma(\bar{t}) \text{ for some } \bar{t} \leqslant t, \\ 0 & \text{otherwise.} \end{cases} \tag{2.5}$$

Eq. (2.5) is our evolution law for the concentration. It says that diffusion into the grain boundary is instantaneous and that solute is left behind in the crystal as the grain boundary migrates. A possible scenario is depicted in Fig. 3, in which the dashed line denotes the initial grain boundary, the solid line the grain boundary at time $t > 0$ and the hashed region contains solute. Note that the normal arrows in this figure always have the same orientation with respect to to the curve Γ. This morphology arises from an initial curved grain boundary (dashed line) with initial concentration such that either there is a single transition point on the initial boundary, so that as time evolves the part of the boundary to the left of the transition point moves upwards and the part to the right moves downwards or there is a middle region in which the curve moves according to curvature with no forcing. See, for example, the numerical computations displayed in Figs. 11 and 14.

If initially there is no concentration in the crystal then there is no jump in concentration to provide a driving force. The direction of the motion is also ambiguous. Our model (2.4), (2.5) requires initial conditions which are the initial location of the interface and that the initial concentration is defined everywhere. We now give an example of initial conditions. Suppose that the initial grain boundary is $\Gamma(0)$. We suppose that the film is unalloyed so that the concentration is zero away from the grain boundary apart from a very

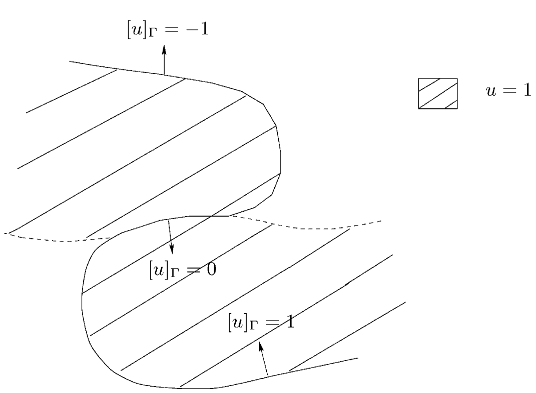

Fig. 3. Jump in concentration.

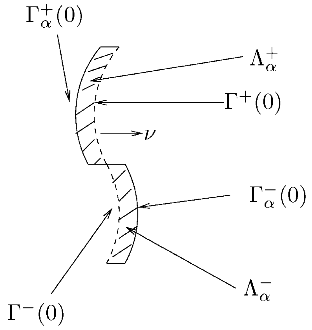

Fig. 4. Initial data.

small region in the neighbourhood of $\Gamma(0)$. That is, in order to initiate bidirectional motion we impose initial data on u such that

$$u(\mathbf{x},0) = \begin{cases} 1 & \forall \mathbf{x} \in \mathscr{R} := \{\Lambda^+_\alpha \cup \Lambda^-_\alpha\}, \\ 0 & \forall \mathbf{x} \in \Omega \setminus \mathscr{R}, \end{cases} \tag{2.6}$$

where Λ^+_α and Λ^-_α, respectively, denote strips of width α lying parallel to $\Gamma(0)$ such that Λ^+_α lies on the negative normal side of $\Gamma^+(0)$ and Λ^-_α lies on the positive normal side of $\Gamma^-(0)$, see Fig. 4. Thus we have partitioned the initial interface $\Gamma(0)$ into $\Gamma^+(0)$ evolving in the positive normal direction and $\Gamma^-(0)$ evolving in the negative normal direction. From the mathematical point of view α is required to be positive but can be arbitrarily small. The choice of $\Lambda^\pm_\alpha$ determines the subsequent evolution. From the computational point of view we will see that α has to be at least the order of a grid size in order for the numerical schemes to observe $\Lambda^\pm_\alpha$.

Clearly the problem (2.4)–(2.6) is a novel initial value problem for interface evolution. It is not clear that a general existence theory could be set out. However in the following we set out a parametric formulation in Section 2.1 and develop a phase field model in Section 2.2. A level set formulation of the sharp interface model is proposed in Section 2.3. These provide the basis for computational models.

2.1. Sharp interface model

Using a parameterization $\mathbf{X}(p,t) = (x(p,t), y(p,t))$ of $\Gamma(t)$, where p is a spatial parameter and t is time as in [6], (2.4) takes the form

$$\mathbf{X}_t = \frac{\mathbf{X}_{pp}}{|\mathbf{X}_p|^2} - [u]_\Gamma \frac{\mathbf{X}_p^\perp}{|\mathbf{X}_p|}, \tag{2.7}$$

where

$$\mathbf{X} : [0,1] \times [0,T] \to \mathbb{R}^2, \quad (p,t) \to \mathbf{X}(p,t),$$

and $(\beta_1,\beta_2)^\perp = (\beta_2, -\beta_1)$. Furthermore (2.5) amounts to setting

$$u(\mathbf{x},t) = \begin{cases} 1 & \text{if either } \exists \bar{t} < t \text{ and } \bar{p} \in [0,1] : \mathbf{X}(\bar{p},\bar{t}) = \mathbf{x}, \ \text{ for } t > 0 \text{ or } u(\mathbf{x},0) = 1, \\ 0 & \text{otherwise.} \end{cases} \tag{2.8}$$

For initial data we set $\mathbf{X}(p,0)$ to be a parameterization of $\Gamma(0)$ and

$$u(\mathbf{x},0)=\begin{cases}1 & \forall\mathbf{x}\in\mathscr{R}:=\{\Lambda_\alpha^+\cup\Lambda_\alpha^-\},\\ 0 & \forall\mathbf{x}\in\Omega\setminus\mathscr{R}.\end{cases}\tag{2.9}$$

Since we are studying a closed curve we require that

$$\mathbf{X}(p,t)=\mathbf{X}(1+p,t)\quad\forall p.\tag{2.10}$$

Remark. To model a single grain boundary that spans the width of Ω and meets the boundaries $x=0$ and $x=L_x$ orthogonally we simply replace (2.10) with the following boundary conditions for $\mathbf{X}=(x(p,t),y(p,t))$:

$$x(0,t)=0,\quad x(1,t)=L_x,\quad y_p(0,t)=y_p(1,t)=0.\tag{2.11}$$

2.2. Phase field model

We propose the following phase field model for bidirectional chemically induced grain boundary motion:

$$\varphi_t-\Delta\varphi-\frac{1}{\varepsilon^2}\varphi+\beta(\varphi)-\frac{\pi\mathscr{F}[u,\varphi]}{4\varepsilon}\ni 0\quad\text{in }\Omega\times(0,T),\tag{2.12}$$

$$\mathscr{F}[u,\varphi]=u(\mathbf{x}+\delta_\varphi^+\mathbf{v}_\varphi,t)-u(\mathbf{x}-\delta_\varphi^-\mathbf{v}_\varphi,t),\tag{2.13}$$

$$\gamma u_t+\tilde{\beta}(u)-(1-\varphi^2)\ni 0\quad\text{in }\Omega\times(0,T)\tag{2.14}$$

with $0<\gamma\ll 1$, $\mathbf{v}_\varphi=\nabla\varphi/|\nabla\varphi|$,

$$\delta_\varphi^\pm=\min r:r\in\left\{r\in\mathbb{R}^+:|\varphi(\mathbf{x}\pm r\mathbf{v}_\varphi)|=\pm 1\right\}$$

and

$$\beta(r)=\begin{cases}(-\infty,0] & \text{for } r=-1,\\ 0 & \text{for } |r|<1,\\ [0,\infty) & \text{for } r=1,\end{cases}\qquad \tilde{\beta}(r)=\begin{cases}0 & \text{for } r<1,\\ [0,\infty) & \text{for } r=1,\\ \infty & \text{for } r>1.\end{cases}$$

Here u and φ are dimensionless field variables with $u\in[0,1]$ representing the concentration of solute atoms in the film and $-1\leqslant\varphi\leqslant 1$ distinguishing the two crystals. The grain boundary is represented by the interfacial region $\Omega_\Gamma:=\{-1<\varphi<1\}$ with width $\mathcal{O}(\varepsilon)$ such that φ takes the value $+1$ on one side of the grain boundary and -1 on the other side. Eq. (2.12) is a double obstacle Allen Cahn equation, see [1], with a non-local forcing term $\mathscr{F}[u,\varphi]$ that mimics the jump in concentration across the interfacial region. The choice of $\delta_\varphi^\pm$ allows the testing of the values of the concentration on either side of the diffuse interfacial region in the normal direction. The scaling is chosen so that interface asymptotics $\varepsilon\to 0$ formally yield (2.4). The order parameter φ takes the value ± 1 exactly outside a narrow diffuse interfacial region whose width as $\varepsilon\to 0$ is $\pi\varepsilon$. On the other hand (2.14) is a time relaxation of (2.5) with relaxation time γ. For initial data we define $d(\mathbf{x})=\operatorname{dist}(\mathbf{x},\Gamma(0))$ and set

$$\varphi(\mathbf{x},0)=\begin{cases}-1 & \text{for } d(\mathbf{x})\leqslant-\frac{\varepsilon\pi}{2},\\ \sin\left(\frac{d(\mathbf{x})}{\varepsilon}\right) & \text{for } -\frac{\varepsilon\pi}{2}<d(\mathbf{x})<\frac{\varepsilon\pi}{2},\\ 1 & \text{for } d(\mathbf{x})\geqslant\frac{\varepsilon\pi}{2},\end{cases}\tag{2.15}$$

$$u(\mathbf{x},0) = \begin{cases} 1 & \forall \mathbf{x} \in \mathscr{R} := \left\{ \Lambda^{+}_{\frac{\varepsilon\pi}{2}} \cup \Lambda^{-}_{\frac{\varepsilon\pi}{2}} \right\}, \\ 0 & \forall \mathbf{x} \in \Omega \setminus \mathscr{R} \end{cases} \tag{2.16}$$

and we impose the boundary condition

$$\frac{\partial \varphi}{\partial \boldsymbol{v}} = 0 \quad \text{on } \partial\Omega \times (0,T). \tag{2.17}$$

Weak formulations of (2.12) and (2.14) take the respective forms

$$\int_{\Omega} ((\eta - \varphi)\varphi_t + \nabla\varphi \cdot \nabla(\eta - \varphi))\,\mathrm{d}\mathbf{x} \geqslant \int_{\Omega} \left(\frac{\varphi}{\varepsilon^2} + \frac{\pi\mathscr{F}[u,\varphi]}{4\varepsilon} \right)(\eta - \varphi)\,\mathrm{d}\mathbf{x} \quad \forall \eta \in K, \tag{2.18}$$

$$\int_{\Omega} \left(\gamma u_t - (1 - \varphi^2)\right)(\eta - u)\,\mathrm{d}\mathbf{x} \geqslant 0 \quad \forall \eta \in \widetilde{K}, \tag{2.19}$$

where

$$K = \{\eta \in H^1(\Omega) : |\eta| \leqslant 1 \text{ in } \Omega\} \quad \text{and} \quad \widetilde{K} = \{\eta \in H^1(\Omega) : \eta \leqslant 1 \text{ in } \Omega\}.$$

Remark 1. We note that the model (2.12)–(2.17) also holds for the setup of a single grain boundary spanning the width of Ω and meeting the faces $x = 0$ and $x = L_x$ orthogonally.

Remark 2. An alternative to (2.14) is to impose

$$u(\mathbf{x},t) = \begin{cases} 1 & \text{if either } \exists \bar{t} \leqslant t : |\varphi(\mathbf{x},\bar{t})| < \frac{\varepsilon_{\varphi}}{2}, \text{ or } u(\mathbf{x},0) = 1, \\ 0 & \text{otherwise.} \end{cases}$$

Taking $\varepsilon_{\varphi} = 0$ would be a phase field analogue of (2.5).

This kind of model for approximating (2.5) is used in the level set computations, see below.

Remark 3. One could also replace (2.14) by a general law

$$\gamma u_t + g(u,\varphi) = 0$$

which drives u to 1 in the interfacial region $|\varphi| < 1$. For example one could take

$$g(u,\varphi) = (u-1)(1-\varphi^2)$$

which is a form of the following Newton law:

$$u_t = m(\varphi)(1-u)$$

for mass transfer between the vapour and the film. Here the mass transfer coefficient $m(\varphi)$ is non-zero only in the grain boundary.

2.3. Level set model

We now define a level set formulation of the sharp interface model. The grain boundary Γ is denoted by the zero set of a sufficiently smooth function $\omega : \mathbb{R}^2 \times (0,T) \to \mathbb{R}$ so that $\Gamma = \{\mathbf{x} \in \mathbb{R}^2 : \omega(\mathbf{x},t) = 0\}$. From [14] we have that if Γ moves with a known speed F then the evolution equation for ω is given by

$\omega_t + F|\nabla\omega| = 0$. Mimicking the jump in concentration across Γ by $\mathscr{F}[u,\omega]$ similar to the forcing term $\mathscr{F}$ proposed in the phase field model we arrive at the following evolution equation for ω:

$$\omega_t - |\nabla\omega|\mathscr{F}[u,\omega] = |\nabla\omega|\nabla\cdot\left(\frac{\nabla\omega}{|\nabla\omega|}\right). \tag{2.20}$$

Since we are only interested in the value of ω in a small neighbourhood of the curve Γ when solving (2.20) we adopt a narrow band/reinitialization approach of the kind presented computationally in [14]. Using this approach we solve (2.20) in a narrow band of width 2ε, $0 < \varepsilon \ll 1$. To ensure that Γ is always contained in the narrow band once it gets within a certain distance of the band's boundary a re-initialization procedure is implemented whereby a new band is calculated by solving the eikonal equation

$$|\nabla\omega| = 1. \tag{2.21}$$

Outside the band we set $\omega = \pm\varepsilon$ accordingly. We calculate the forcing term inside the band using

$$\mathscr{F}[u,\omega] = u(\mathbf{x} + \delta^{+}_{\omega}\boldsymbol{v}_{\omega}, t) - u(\mathbf{x} - \delta^{-}_{\omega}\boldsymbol{v}_{\omega}, t), \tag{2.22}$$

where $\boldsymbol{v}_{\omega} = \nabla\omega/|\nabla\omega|$ and

$$\delta^{\pm}_{\omega} = \min r : r \in \{r \in \mathbb{R}^{+} : |\omega(\mathbf{x} \pm r\boldsymbol{v}_{\omega})| = \pm\varepsilon\}.$$

Furthermore, we set

$$u(\mathbf{x},t) = \begin{cases} 1 & \text{if either } \exists \bar{t} \leqslant t : |\omega(\mathbf{x},\bar{t})| < \frac{\varepsilon_\omega}{2}, \text{ or } u(\mathbf{x},0) = 1, \\ 0 & \text{otherwise.} \end{cases} \tag{2.23}$$

Taking $\varepsilon_\omega = 0$ would be the level set formulation of (2.5). Alternatively we could use the level set version of (2.5) equivalent to the time relaxation used in the phase field model, but for the purpose of this article we use (2.23) with $\varepsilon_\omega = \varepsilon$. For initial data that satisfies (2.6) we define $d(\mathbf{x}) = \mathrm{dist}(\mathbf{x}, \Gamma(0))$ and set

$$\omega(\mathbf{x},0) = \begin{cases} -\varepsilon & \text{for } d(\mathbf{x}) \leqslant -\varepsilon, \\ d(\mathbf{x}) & \text{for } -\varepsilon < d(\mathbf{x}) < \varepsilon, \\ \varepsilon & \text{for } d(\mathbf{x}) \geqslant \varepsilon, \end{cases} \quad u(\mathbf{x},0) = \begin{cases} 1 & \forall \mathbf{x} \in \mathscr{R} := \{\Lambda^{+}_{\varepsilon} \cup \Lambda^{-}_{\varepsilon}\}, \\ 0 & \forall \mathbf{x} \in \Omega \setminus \mathscr{R} \end{cases} \tag{2.24}$$

and we impose the boundary condition

$$\frac{\partial\omega}{\partial\boldsymbol{v}} = 0 \quad \text{on } \partial\Omega \times (0,T). \tag{2.25}$$

3. Numerical discretizations

In this section we derive numerical approximations of the sharp interface, phase field and level set models presented in Section 2.

3.1. Sharp interface model

We discretize the parametric formulation of the sharp interface model (2.7), (2.8) using the mass lumping approach first introduced in [7], this gives the following difference scheme for $j = 1, \ldots, M-1$:

$$\frac{1}{2\Delta t}((h^n_{j+1})^2 + (h^n_j)^2)(\mathbf{X}^{n+1}_j - \mathbf{X}^n_j) = \mathbf{X}^{n+1}_{j+1} - 2\mathbf{X}^{n+1}_j + \mathbf{X}^{n+1}_{j-1} - \frac{h^n_{j+1}}{2}\Big((\mathbf{X}^n_{j+1})^\perp - (\mathbf{X}^n_j)^\perp\Big)\mathscr{F}_j\big[u^n_h, \mathbf{X}^n_h\big]$$
$$- \frac{h^n_j}{2}\Big((\mathbf{X}^n_j)^\perp - (\mathbf{X}^n_{j-1})^\perp\Big)\mathscr{F}_j\big[u^n_h, \mathbf{X}^n_h\big], \tag{3.1}$$

where $h^n_j = |\mathbf{X}^n_j - \mathbf{X}^n_{j-1}|$ and $\mathscr{F}_j[u^n_h, \mathbf{X}^n_h]$ which is defined later is an approximation to the jump in concentration across $\mathbf{X}$. Here $\mathbf{X}^n_j = (x^n_j, y^n_j) = \mathbf{X}(s_j, t)$ for all $t \in [n\Delta t, (n+1)\Delta t)$, $j = (0, \dots, M)$ is the discrete solution and each $\mathbf{X}_j = (x_j, y_j)$ is a vector in $\mathbb{R}^2$ with

$$\mathbf{X}^n_0 = \mathbf{X}^n_{\mathrm{M}} \quad \forall n > 0.$$

In order to evaluate a discrete form of (2.7) we require values of $u^n_h(\mathbf{x})$ for all $\mathbf{x} \in \Omega$ and not just for values of $\mathbf{x}$ on the interface Γ. Thus we introduce a 'background' fine, uniform mesh $\mathscr{M}$ with grid size $\tilde{h}$ and for any $\mathbf{x} \in \Omega$ we define $(\mathbf{x})^m$ to be its nearest node on $\mathscr{M}$. This enables us to approximate $[u]_\Gamma$ by

$$\mathscr{F}_j\big[u^n_h, \mathbf{X}^n_h\big] = u^n_h\Big((\mathbf{X}^n_j + \delta \boldsymbol{v}^n_j)^m\Big) - u^n_h\Big((\mathbf{X}^n_j - \delta \boldsymbol{v}^n_j)^m\Big), \tag{3.2}$$

where $\boldsymbol{v}^n_j = (\mathbf{X}^n_j)^\perp_s / |(\mathbf{X}^n_j)_s|$ with $(\mathbf{X}^n_j)^\perp_s = \Big(y^n_{j+1} - y^n_{j-1}, x^n_{j+1} - x^n_{j-1}\Big)$. We choose δ to be $\mathscr{O}(\tilde{h})$ so that we test the values of u^n_h on either side of the interface. We update $u^{n+1}_h(\mathbf{x})$ for all $\mathbf{x} \in \mathscr{M}$ in the following way:

$$u^{n+1}_h(\mathbf{x}) = \begin{cases} 1 & \text{if } \mathbf{x} \in \mathscr{S}_i,\ i = 0, \dots, M-1, \\ u^n_h(\mathbf{x}) & \text{otherwise,} \end{cases}$$

where $\mathscr{S}_i$ denotes the area enclosed by the four lines that join the points $(\mathbf{X}^n_i)^m$ and $(\mathbf{X}^{n+1}_i)^m$, $(\mathbf{X}^n_{i+1})^m$ and $(\mathbf{X}^{n+1}_{i+1})^m$, $(\mathbf{X}^n_i)^m$ and $(\mathbf{X}^n_{i+1})^m$ and $(\mathbf{X}^{n+1}_i)^m$ and $(\mathbf{X}^{n+1}_{i+1})^m$, see Fig. 5.

Remark. For the case of a single grain boundary spanning the width of Ω satisfying (2.11) we use the techniques introduced in [5] to obtain

$$x^{n+1}_0 = 0, \quad x^{n+1}_{\mathrm{M}} = L_x, \tag{3.3}$$

$$\frac{1}{2\Delta t}(h^n_1)^2(y^{n+1}_0 - y^n_0) = (y^{n+1}_1 - y^{n+1}_0) - \frac{h^n_1}{2}\big((x^n_1)^\perp - (x^n_0)^\perp\big)\mathscr{F}_0\big[u^n_h, \mathbf{X}^n_h\big],$$

$$\frac{1}{2\Delta t}(h^n_M)^2(y^{n+1}_M - y^n_{\mathrm{M}}) = (y^{n+1}_{M-1} - y^{n+1}_{\mathrm{M}}) - \frac{h^n_{\mathrm{M}}}{2}\big((x^n_M)^\perp - (x^n_{M-1})^\perp\big)\mathscr{F}_{M-1}\big[u^n_h, \mathbf{X}^n_h\big].$$

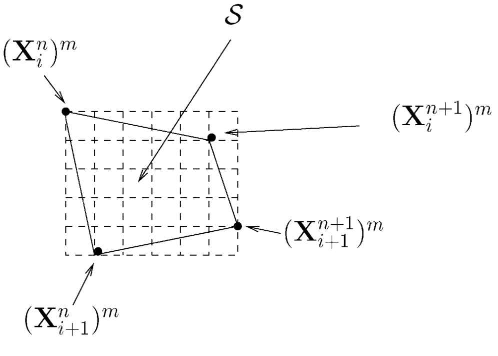

Fig. 5. Updating u^n_h.

3.2. Phase field model

Before we derive a numerical discretization of the phase field model (2.18), (2.19) we introduce some useful notation.

We set $\mathscr{T}_h$ to be a quasi-uniform triangulation of Ω with $h := \max_{T\in\mathscr{T}_h} \operatorname{diam}(T)$ and we denote by $\mathscr{N}_h = \{\mathbf{x}_1, \ldots, \mathbf{x}_\mathrm{M}\}$ the set of nodes of $\mathscr{T}_h$ with $\{\xi_1, \ldots, \xi_\mathrm{M}\}$ denoting the corresponding standard basis of S_h, where

$$S_h := \left\{\chi \in C^0(\overline{\Omega}) : \chi \text{ is linear on each } T \in \mathscr{T}_h\right\}.$$

Furthermore, we set

$$K_h := \{\eta \in S_h : |\eta(x)| \leqslant 1 \text{ for all } x \in \Omega\} \quad \text{and} \quad \widetilde{K}_h := \{\eta \in S_h : \eta(x) \leqslant 1 \text{ for all } x \in \Omega\},$$

and we let $\Delta t > 0$ be a time step with $t_n = n\Delta t,\ n \geqslant 0$.

Finally for a given node $\mathbf{x}_j$ we denote by C_j the set of nodes directly adjacent to $\mathbf{x}_j$ and we split $\mathscr{N}_h$ into three sets, $\mathscr{N}^n_\Gamma$, $\mathscr{N}^n_+$ and $\mathscr{N}^n_-$, where

$$\mathscr{N}^n_\pm = \{\mathbf{x}_j \in \mathscr{N}_h : \varphi^n_j = \pm 1 \text{ and } \varphi^n_k = \pm 1 \text{ for all nodes } \mathbf{x}_k \in C_j\},$$

$$\mathscr{N}^n_\Gamma = \mathscr{N}_h \setminus [\mathscr{N}^n_+ \cup \mathscr{N}^n_-].$$

From the above definitions we see that the nodes $\mathbf{x}_j \in \mathscr{N}^n_\Gamma$ are situated in a discrete approximation of the interfacial region $\Omega_\Gamma(t) = \{-1 < \varphi < 1\}$, while the nodes $\mathbf{x}_j \in \mathscr{N}^n_+$ and $\mathbf{x}_j \in \mathscr{N}^n_-$ are situated in discrete approximations of regions where $\varphi(\mathbf{x}, t) = 1$ and $\varphi(\mathbf{x}, t) = -1$, respectively.

We now derive a finite element approximation of (2.18), (2.19):

Find $\{\varphi^{n+1}_h, u^{n+1}_h\} \in K_h \times \widetilde{K}_h$ such that

$$\frac{1}{\Delta t}\left(\varphi^{n+1}_h - \varphi^n_h, \eta - \varphi^{n+1}_h\right)_h + \int_\Omega \nabla\varphi^n_h \cdot \nabla(\eta - \varphi^{n+1}_h) \geqslant \left(\frac{\varphi^n_h}{\varepsilon^2} + \frac{\pi\mathscr{F}\left[u^n_h, \varphi^n_h\right]}{4\varepsilon}, \eta - \varphi^{n+1}_h\right)_h \quad \forall\eta \in K_h, \tag{3.4}$$

$$\left(u^{n+1}_h - u^n_h, \eta - u^{n+1}_h\right)_h - \gamma\Delta t\left(1 - (\varphi^n_h)^2, \eta - u^{n+1}_h\right)_h \geqslant 0 \quad \forall\eta \in \widetilde{K}_h, \tag{3.5}$$

where for each node $\mathbf{x}_j$ of $\mathscr{T}_h$

$$\mathscr{F}_j\left[u^n_h, \varphi^n_h\right] = u^n(\mathbf{x}_{k^+}) - u^n(\mathbf{x}_{k^-}),$$

with

$$\mathbf{x}_{k^\pm} = (\mathbf{x}_j \pm \delta^\pm_\varphi v_\varphi)^m$$

such that

$$\delta^\pm_\varphi = \min r : r \in \left\{r \in \mathbb{R}^+ : (\mathbf{x}_j \pm r v_\varphi)^m \in \mathscr{N}^n_\pm\right\}$$

and for any $\mathbf{x} \in \Omega$ we define $(\mathbf{x})^m$ to be the nearest node in $\mathscr{N}_h$. Here $(\cdot,\cdot)_h$ denotes the discrete inner product on $L^2(\Omega)$, defined by

$$(\eta_1, \eta_2)_h := \int_\Omega \Pi^h(\eta_1\eta_2)\,\mathrm{d}\mathbf{x},$$

where $\Pi^h : C(\overline{\Omega}) \to S_h$ is the standard piecewise linear interpolation operator.

We may view ε as an approximation parameter for the sharp interface problem and in order to resolve the interfacial region we set $h \ll \varepsilon$. Note that if $h \simeq \pi\varepsilon/N$ then there are approximately N grid points spanning the diffuse interface. Since the discretization (3.4) is explicit in time and the only term involving φ_h^{n+1} is the lumped mass L^2 inner product it is well known that the discrete variational inequality (3.4) can be solved in the following way. First we calculate the explicit equation update $\tilde{\varphi}_h^{n+1}$ by solving

$$\frac{1}{\Delta t}(\tilde{\varphi}_h^{n+1} - \varphi_h^n, \eta)_h + \int_\Omega \nabla\varphi_h^n \cdot \nabla\eta = \left(\frac{\varphi_h^n}{\varepsilon^2} + \frac{\pi\mathscr{F}\left[u_h^n, \varphi_h^n\right]}{4\varepsilon}, \eta\right)_h \quad \forall\eta \in S_h \tag{3.6}$$

and then we project onto K_h by setting at each node $\mathbf{x}_i$ of the triangulation

$$\varphi_i^{n+1} = \begin{cases} -1 & \text{if } \tilde{\varphi}_i^{n+1} \leqslant -1, \\ \tilde{\varphi}_i^{n+1} & \text{if } -1 < \tilde{\varphi}_i^{n+1} < 1, \\ 1 & \text{if } \tilde{\varphi}_i^{n+1} \geqslant 1, \end{cases} \tag{3.7}$$

where $\varphi_i^{n+1} := \varphi_h^{n+1}(\mathbf{x}_i)$ and $\tilde{\varphi}_i^{n+1} := \tilde{\varphi}_h^{n+1}(\mathbf{x}_i)$. Similarly we solve (3.5) by calculating $\tilde{u}_h^{n+1}$ by solving

$$\left(\tilde{u}_h^{n+1} - u_h^n, \eta\right)_h = \gamma\Delta t\left(1 - (\varphi_h^n)^2, \eta\right)_h$$

and then projecting onto $\widetilde{K}_h$ by setting at each node $\mathbf{x}_i$ of the triangulation

$$u_i^{n+1} = \begin{cases} \tilde{u}_i^{n+1} & \text{if } \tilde{u}_i^{n+1} < 1, \\ 1 & \text{if } \tilde{u}_i^{n+1} \geqslant 1. \end{cases}$$

For the initial data $\varphi_h^0(\mathbf{x})$ and $u_h^0(\mathbf{x})$ we use interpolates of (2.15) and (2.16). Setting $\eta = \xi_j$ in (3.5) yields

$$u_j^{n+1} = u_j^n \quad \forall\mathbf{x}_j \in \mathscr{N}_+^n \cup \mathscr{N}_-^n \tag{3.8}$$

and hence we only need to solve (3.5) for all $\mathbf{x}_j \in \mathscr{N}_\Gamma^n$. Similarly setting $\eta = \xi_j$ in (3.6) it follows that:

$$\tilde{\varphi}_j^{n+1} = 1 + \frac{\Delta t}{\varepsilon^2}\left(1 + \frac{\pi\varepsilon}{4}\mathscr{F}_j\left[u_h^n, \varphi_h^n\right]\right) \quad \forall\mathbf{x}_j \in \mathscr{N}_+^n,$$

$$\tilde{\varphi}_j^{n+1} = -1 - \frac{\Delta t}{\varepsilon^2}\left(1 - \frac{\pi\varepsilon}{4}\mathscr{F}_j\left[u_h^n, \varphi_h^n\right]\right) \quad \forall\mathbf{x}_j \in \mathscr{N}_-^n.$$

Choosing ε sufficiently small such that $1 \geqslant (\pi\varepsilon/4)\max|\mathscr{F}| = \frac{\pi\varepsilon}{4}$ (since $|\mathscr{F}[u, \varphi]| \leqslant 1$) from (3.7) we conclude

$$\left.\begin{array}{ll} \tilde{\varphi}_j^{n+1} \leqslant -1 & \text{if } \varphi_j^n = -1 \\ \tilde{\varphi}_j^{n+1} \geqslant 1 & \text{if } \varphi_j^n = 1 \end{array}\right\} \Rightarrow \varphi_j^{n+1} = \varphi_j^n \quad \forall\mathbf{x}_j \in \mathscr{N}_+^n \cup \mathscr{N}_-^n.$$

Thus we only need to solve (3.4) for all $\mathbf{x}_j \in \mathscr{N}_\Gamma^n$. The condition $\varepsilon \leqslant 4/\pi$ is not a restriction on ε from a practical point of view. For stability of the scheme (3.4) we require $\Delta t \leqslant C_\mathrm{m}h^2$, where C_m is a mesh constant. In the case of a uniform right-angled isosceles triangulation $C_\mathrm{m} = 1/4$.

3.3. Level set model

We discretize a regularized version of (2.20) on a uniform grid, with mesh size h and time step Δt, using a second-order central finite difference approximation on the right-hand side and an upwind scheme on the left-hand side, see [2] for a finite difference scheme for the motion of level set surfaces by mean curvature and [14] for level set discretizations in general. Setting $[v]_+ := \max(v, 0)$ and $[v]_- := \min(v, 0)$, for $\tilde{\varepsilon} \ll 1$ this yields the following:

$$\frac{1}{\Delta t}(\omega_{ij}^{n+1} - \omega_{ij}^{n}) = \left(\left[\mathscr{F}_{ij}^{n}\right]_{-}\nabla^{+}(\omega_{ij}^{n}) + \left[\mathscr{F}_{ij}^{n}\right]_{+}\nabla^{-}(\omega_{ij}^{n})\right) + |\nabla(w_{ij}^{n})|\kappa_{ij}^{n}, \tag{3.9}$$

where (suppressing the superscript n)

$$\nabla^{\pm}(\omega_{ij}) = \left([(\omega_{ij})^{\mp x}]_{+}^{2} + [(\omega_{ij})^{\pm x}]_{-}^{2} + [(\omega_{ij})^{\mp y}]_{+}^{2} + [(\omega_{ij})^{\pm y}]_{-}^{2}\right)^{1/2},$$

with

$$(\omega_{ij})^{\pm x} = \pm\frac{(\omega_{i\pm 1j} - \omega_{ij})}{h}, \quad (\omega_{ij})^{\pm y} = \pm\frac{(\omega_{ij\pm 1} - \omega_{ij})}{h}$$

and standard central differences were used to approximate

$$|\nabla w_{ij}|\kappa_{ij} = |\nabla w_{ij}|\nabla\cdot\left(\frac{\nabla\omega_{ij}}{\left(|\nabla\omega_{ij}|^{2} + \bar{\varepsilon}^{2}\right)^{\frac{1}{2}}}\right).$$

The parameter $\bar{\varepsilon} = \mathscr{O}(h)$ is introduced to avoid dividing by zero.

In order to approximate (2.23) we set

$$u_{ij}^{n} = \begin{cases} 1 & \text{if } |\omega_{ij}^{n}| < \frac{\varepsilon}{2}, \\ 0 & \text{otherwise} \end{cases} \tag{3.10}$$

and when discretizing (2.22) we adapt the approach formulated in the phase field discretization and set for each grid point $\mathbf{x}_{ij}$

$$\mathscr{F}_{ij}\left[u_{h}^{n}, \omega_{h}^{n}\right] = u^{n}(\mathbf{x}_{(kl)^{+}}) - u^{n}(\mathbf{x}_{(kl)^{-}}),$$

with

$$\mathbf{x}_{(kl)^{\pm}} = (\mathbf{x}_{ij} \pm \delta_{\omega}^{\pm}v_{ij})^{m}$$

such that

$$\delta_{\omega}^{\pm} = \min r : r \in \left\{r \in \mathbb{R}^{+} : (\mathbf{x}_{ij} \pm r v_{ij})^{m} \in \mathscr{N}_{\pm}^{n}\right\}$$

with

$$\boldsymbol{v}_{ij} = \frac{\left(\omega_{i+1j}^{n} - \omega_{i-1j}^{n}, \omega_{ij+1}^{n} - \omega_{ij-1}^{n}\right)}{\left((\omega_{i+1j}^{n} - \omega_{i-1j}^{n})^{2} + (\omega_{ij+1}^{n} - \omega_{ij-1}^{n})^{2}\right)^{1/2}}.$$

Here for any $\mathbf{x} \in \Omega$ we define $(\mathbf{x})^{m}$ to be its nearest node in the uniform grid $\mathscr{N}$, and we denote

$$\mathscr{N}_{\pm}^{n} = \{\mathbf{x}_{ij} \in \mathscr{N} : \omega_{ij}^{n} = \pm\varepsilon \text{ and } \omega_{kl}^{n} = \pm\varepsilon \text{ for all grid points } \mathbf{x}_{kl} \in \{\mathbf{x}_{i-1j}, \mathbf{x}_{i+1j}, \mathbf{x}_{ij-1}, \mathbf{x}_{ij+1}\}\}.$$

In [2] a stability analysis of an explicit time discretization for a level set approach to mean curvature flow indicates that for stability we require $\Delta t \leqslant C_{\mathrm{M}} h^2$. We solve (3.9) and (3.10) using the narrow band/re-initialization procedure.

Step 1. Set $0 < \hat{\varepsilon} < \varepsilon$ and $0 < \tilde{\varepsilon} < \varepsilon^* < \varepsilon$.

Step 2. Set $\mathscr{B} := \{ij \in \mathscr{N} : |\omega^0_{ij}| < \varepsilon\}$ and $\delta(\mathscr{B}) := \{ij \in \mathscr{B} : |\omega^0_{ij}| > \varepsilon^*\}$.

Step 3. Solve (3.9) and (3.10) for all $ij \in \mathscr{B}$ until there exists a $K \in \mathbb{N}$ such that

$$|\omega^K_{ij}| < \tilde{\varepsilon} \quad \text{for some } ij \in \delta(\mathscr{B}).$$

Step 4. Re-evaluate ω^K_{ij} for all $ij \in \mathscr{N}$ by solving $|\nabla\omega|_h = 1$ (see below) with the boundary condition

$$\omega^K_{ij} = \omega^n_{ij} \quad \text{when } |\omega^n_{ij}| < \hat{\varepsilon}.$$

Step 5. Reset $\mathscr{B} := \{ij \in \mathscr{N} : |\omega^K_{ij}| < \varepsilon\}$ and $\delta(\mathscr{B}) := \{ij \in \mathscr{B} : |\omega^K_{ij}| > \varepsilon^*\}$.

Step 6. Return to Step 3.

A choice of parameters that we have used in the computations below is $\varepsilon, \varepsilon^*, \tilde{\varepsilon}, \hat{\varepsilon}$:

$$\varepsilon = 7h, \quad \varepsilon^* = \frac{3\varepsilon}{4}, \quad \tilde{\varepsilon} = \frac{\varepsilon}{2}, \quad \hat{\varepsilon} = \frac{\varepsilon}{5}.$$

The procedure outlined in Step 3 is known as re-initialization and can be efficiently implemented using the fast marching method defined in [14]. For completeness we include a brief description of the fast marching method; this method allows us to solve (2.21) without iteration. An upwind scheme given in [13] for solving (2.21) is the following:

$$|\nabla\omega|_h := \max((\omega_{ij})^{-x}, -(\omega_{ij})^{+x}, 0)^2 + \max((\omega_{ij})^{-y}, -(\omega_{ij})^{+y}, 0)^2 = 1. \tag{3.11}$$

The idea behind the fast marching method is to systematically construct the solution ω using only upwind values. All grid points in the narrow band with the exception of those where $|\omega^n_{ij}| \leqslant \hat{\varepsilon}$ (for some $\hat{\varepsilon} < \varepsilon$) are updated and the key is the order in which they are updated. In particular the following update procedure is used: First tag all grid points where $|\omega^n_{ij}| \leqslant \hat{\varepsilon}$ as *known*. Then tag as *trial* all points that are one grid point away from a *known* point. Finally tag as *far* all remaining points. Now use the following procedure:

Step 1. Let A be the *trial* point with smallest ω value.

Step 2. Add A to known and remove it from *trial*.

Step 3. Tag all neighbours of A as *trial* if they are not *known*.

Step 4. Recompute the values of ω at all *trial* neighbours of A according to (3.11).

Step 5. Return to Step 1.

4. Numerical results

In this section we present numerical simulations using the three discretizations derived in Section 3. The bulk of the computations reproduces the numerical simulations presented in [10] which illustrate the following three effects associated with bidirectional motion: the formation of double seams, whereby a grain boundary doubles back on itself, a threshold effect between evolutions to stable S-configurations and double seams and the migration of transition points between parts of the grain boundary that move in alternating directions. Examples of these effects are displayed in Figs. 6–9 whose results are obtained using the sharp interface discretization presented in Section 3.1 and take the following form: for each simulation two subplots are presented, in each case the left-hand plots displays the grain boundary evolving in time to some final time $\bar{t}$, while the right-hand plot shows the alloyed region at the final time $\bar{t}$. In the remaining

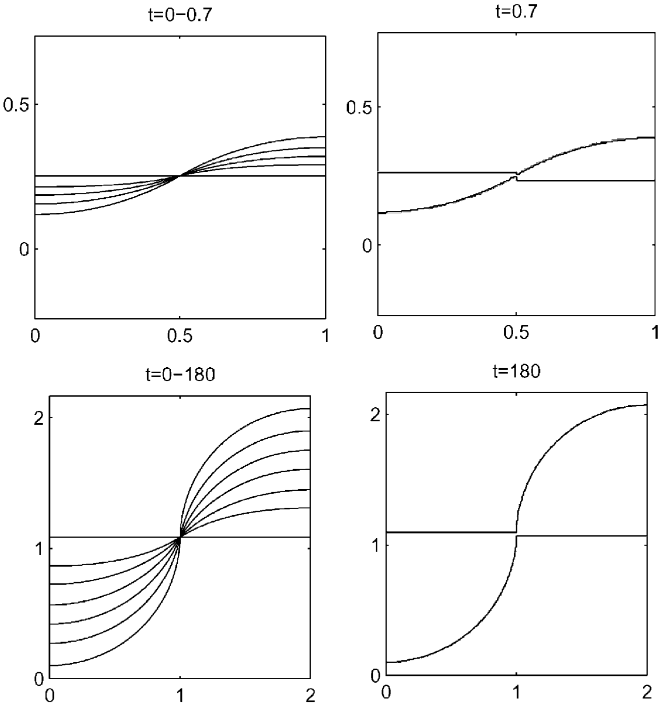

Fig. 6. Sharp interface stationary arc solutions with $L_x = 1$ and $L_x = 2$.

four figures, Figs. 10–13, the approximate solutions of the three models are compared. When comparing sharp interface solutions with either phase field or level set solutions we plot a '$*$' at every $\tilde{n}$th node of the sharp interface discretization and a contour plot of either the phase field order parameter φ or the level set function ω.

Figs. 6 and 7 display the evolution of an initially straight grain boundary $\Gamma(0)$ that spans Ω and is decomposed equally into $\Gamma^+(0)$ and $\Gamma^-(0)$ with a single transition point between the two segments. Due to the natural symmetry of the problem we expect Γ^+ and Γ^- to evolve in time while the transition point between them remains fixed and indeed this is what we see. In [10] it is observed that in such setups if $L_x \leqslant 2$ an exact stationary solution exists that is the arc of a circle of radius 1 pinned to the boundary points (see Fig. 6). Whereas for $L_x > 2$ no such stationary solution exists and the length of the grain boundary increases unboundedly until it hits the boundary of the domain (see Fig. 7).

In Fig. 8 we remove the natural transition point symmetry imposed in the previous figures and display the evolution of a creeping transition point. In the left-hand subplot it can be seen that there are three transitions points which are located 1/3, 1/2 and 2/3 in distance along the initial grain boundary. This gives rise in the middle third to upward (downward) motion directly to the left (right) of the centre point, whilst the remaining two thirds of the boundary moves downward (upward) at the left (right) end. As time evolves the two non-central transition points move towards each other and eventually all three merge. Subsequently the boundary to the left of centre moves downward, whilst the right moves upward. This motion gives rise to the alloyed region depicted in the right-hand subplot. Fig. 9 displays the evolution of a single closed curve grain boundary that initially has six transition points between sections of Γ^+ and Γ^-. We note that the step discontinuities that are observed in the concentration plots, but not the grain boundary plots of Figs. 6–9 arise due to the specific choice of initial data for the concentration, recall (2.6) and Fig. 4.

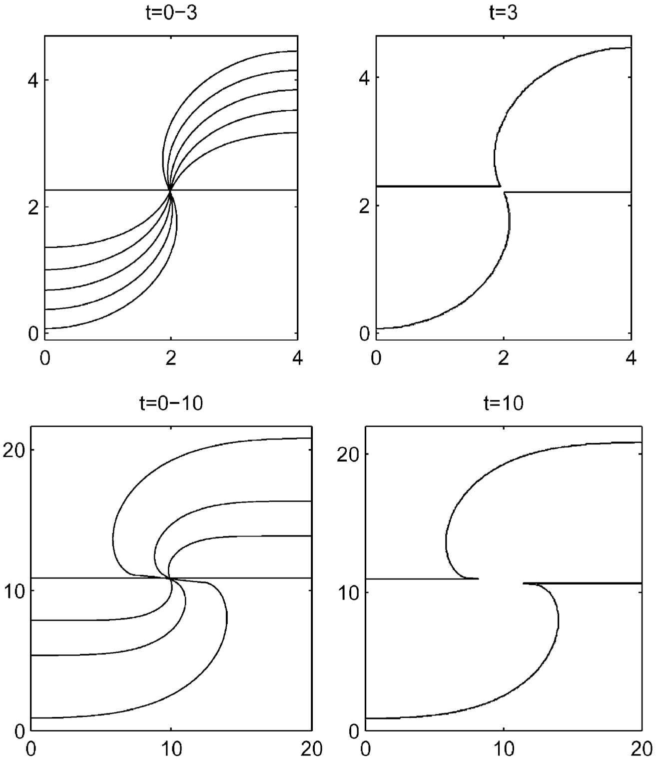

Fig. 7. Evolutionary sharp interface solutions with $L_x = 4$ and $L_x = 20$.

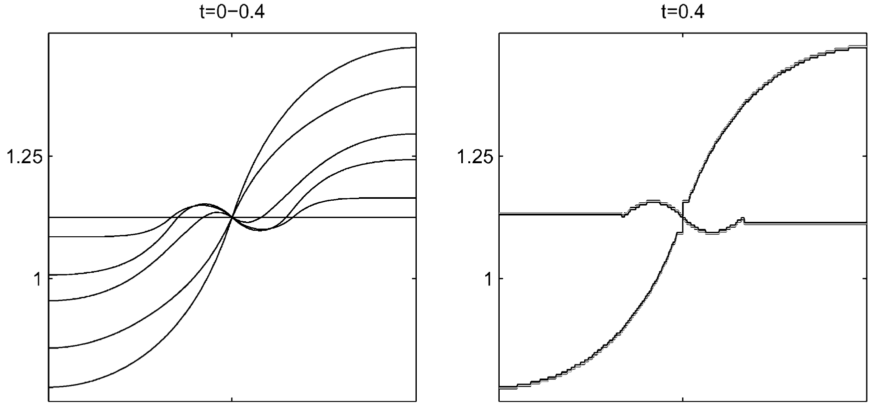

Fig. 8. Evolutionary sharp interface solutions with migrating transition points.

Figs. 10 and 12 compare sharp interface and phase field simulations. In each case the top left-hand subplot displays contour plots of the approximate phase field solution φ while the top right-hand plot displays the approximate sharp interface solution. The bottom subplots compare close-ups of the sharp interface and phase field solutions in two parts of the domain. We do not show a simulation of the con-

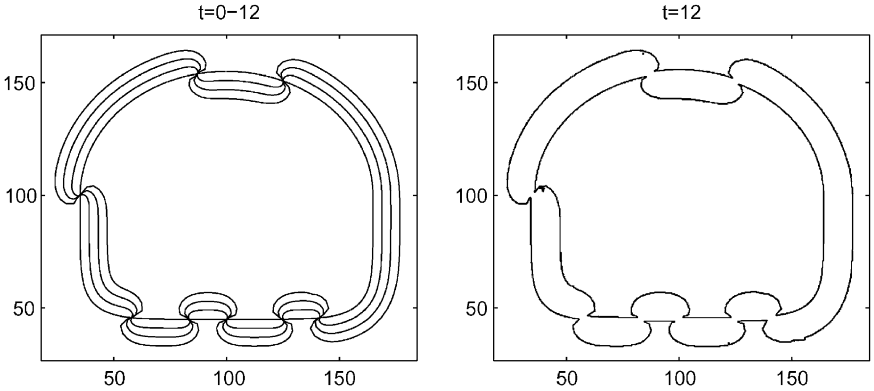

Fig. 9. Evolutionary closed curve sharp interface solutions.

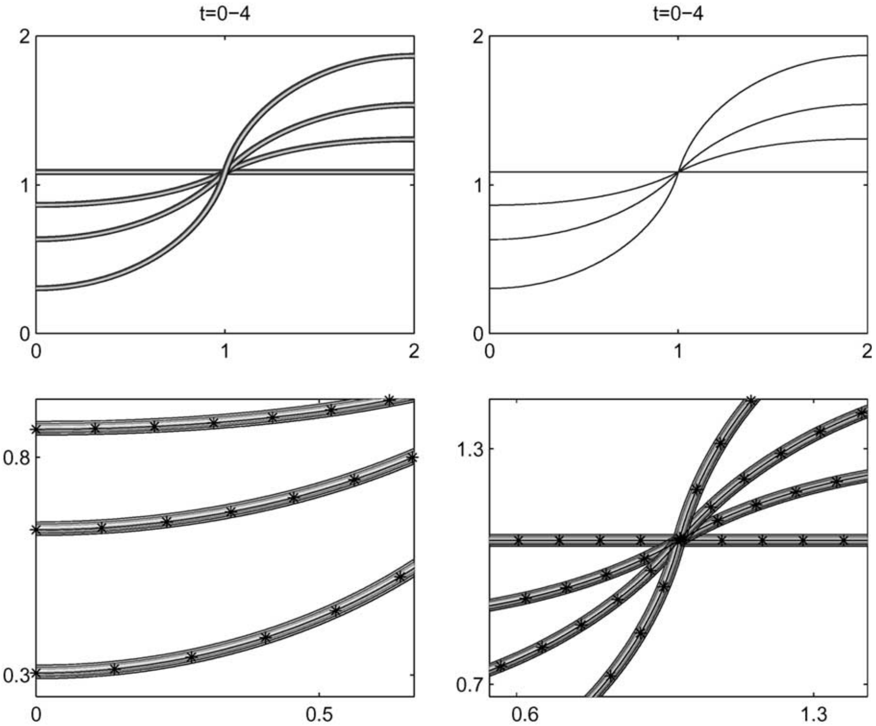

Fig. 10. Comparison of sharp interface and phase field solutions with $L_x = 2$.

centrations for the two models as on the scales shown they are indistinguishable. In Fig. 10 $L_x = 2$, $\Gamma(0)$ is decomposed equally into $\Gamma^+(0)$ and $\Gamma^-(0)$ and the approximate solutions are displayed at times $t = 0, 0.25, 0.75$ and 4. In Fig. 12 $L_x = 3$, $\Gamma(0)$ contains two transition points between $\Gamma^+(0)$ and $\Gamma^-(0)$ and the approximate solutions are displayed at times $t = 0, 0.12, 0.32$ and 0.4.

Figs. 11 and 13 take the same form as Figs. 10 and 12 except that here level set and sharp interface simulations are compared. In Fig. 11 $L_x = 20$, $\Gamma(0)$ is decomposed equally into $\Gamma^+(0)$ and $\Gamma^-(0)$ and the

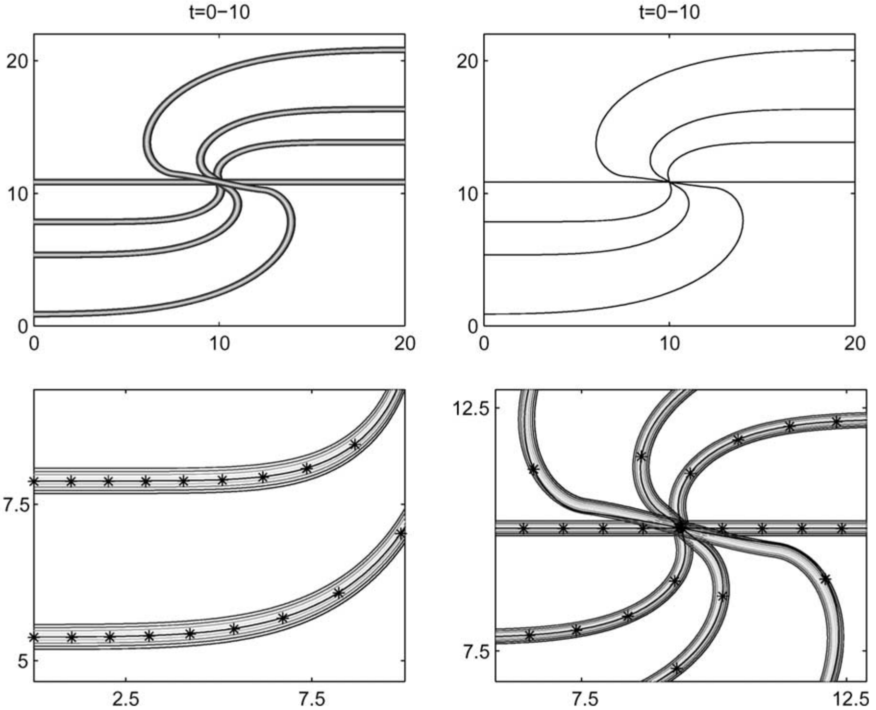

Fig. 11. Comparison of sharp interface and level set solutions with $L_x = 20$.

approximate solutions are displayed at times $t = 0, 3, 5.5$ and 10. In Fig. 13 the approximate solutions are displayed at times $t = 0, 0.2, 0.4$ and 0.6.

Finally, we show a computation, Fig. 14, which yields a morphology similar to Fig. 3. The left-hand subplot shows the initial condition while the right-hand subplot shows the solution at time $t = 11$.

All the phase field and level set simulations are computed using uniform grids with mesh size h, while the background meshes in the sharp interface simulations are uniform grids with mesh size $\tilde{h}$. The values of the discretization parameters $h, \Delta t$, etc. used in the simulations are given in Tables 1 and 2, in which a '-' is used to denote non-applicability.

Remark. Experimental stability analysis of the three schemes yields the following stability results; for stability of the phase field and level set explicit time discretizations we require $\Delta t \leqslant h^2/4$ and $\Delta t \leqslant h^2/2$, respectively, while for the sharp interface semi-implicit discretization it suffices to have $\Delta t \leqslant Ch$.

5. Conclusion

We consider numerically mathematical models for bidirectional grain boundary dynamics in thin films. The problem is reduced to a two-dimensional one for $\mathbf{x} \in \Omega = (0, L_x) \times (0, L_y)$, where Ω corresponds to the top face of the film. We assume that the solute atoms from the vapour surrounding the film diffuse into the film very rapidly such that the concentration $u(\mathbf{x}, t)$ of solute atoms in the film is equal to 1 if the grain boundary has passed through the point $\mathbf{x}$ and 0 otherwise. We present three models; sharp interface, phase field and level set. The simulations show good agreement between the solutions of the three models. Also there is good agreement between the simulations presented here and those seen in [10] where various ex-

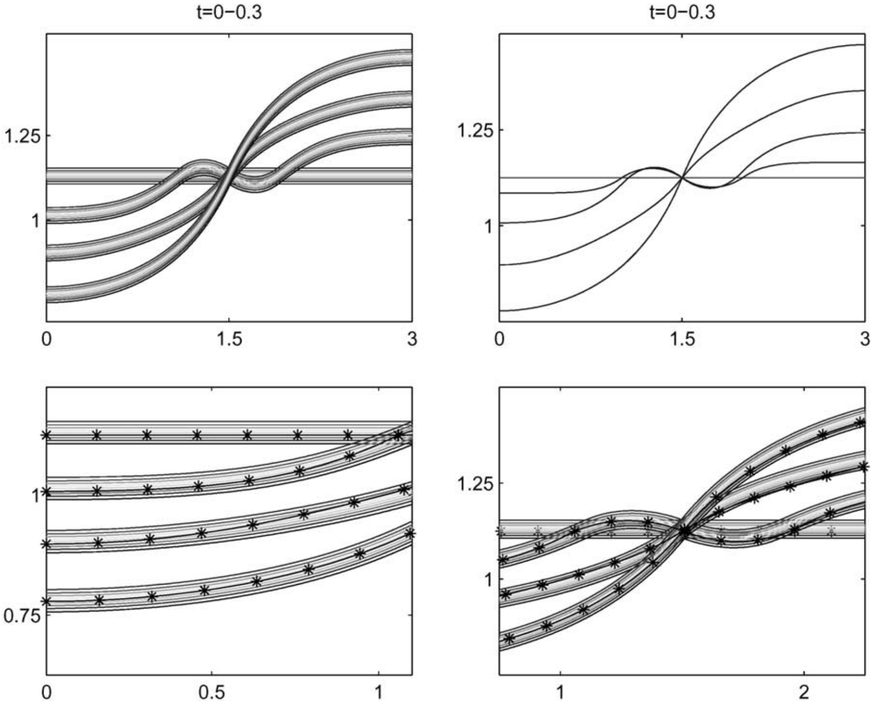

Fig. 12. Comparison of sharp interface and phase field solutions.

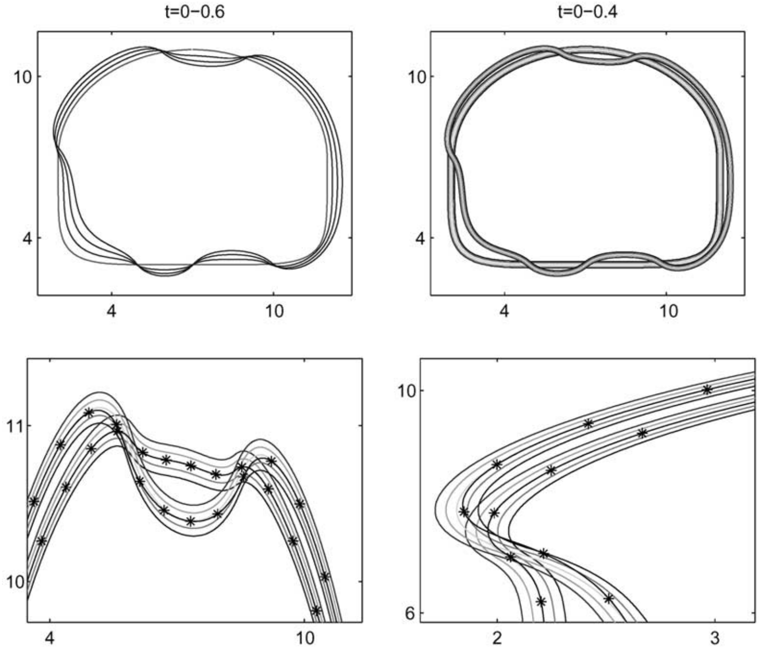

Fig. 13. Comparison of sharp interface and level set solutions.

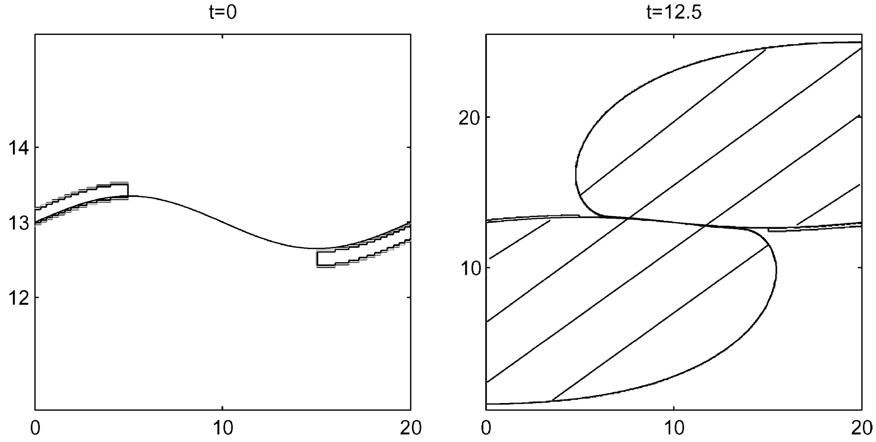

Fig. 14. Morphology similar to that of Fig. 3.

Table 1
Parameters used in sharp interface simulations Figs. 6–9

	M	$h := L_x/M$	Δt	$\tilde{h}$
Fig. 6 – top subplots	200	1/200	$h/4$	1/300
Fig. 6 – bottom subplots	200	1/100	$h/4$	1/300
Fig. 7 – top subplots	200	2/100	$h/4$	1/100
Fig. 7 – bottom subplots	400	1/500	$h/40$	1/30
Fig. 8	200	3/200	$h/20$	1/200
Fig. 9	600	1/3	$h/40$	2/9

Table 2
Parameters used in Figs. 10–13

	Sharp interface				Phase field			Level set				
	M	$h := L_x/M$	Δt	$\tilde{h}$	h	Δt	ε	h	Δt	ε	$\tilde{\varepsilon}$	ε^*
Fig. 10	200	2/100	$h/4$	1/100	1/300	$h^2/4$	0.015	–	–	–	–	–
Fig. 11	400	1/500	$h/40$	1/30	–	–	–	1/30	$h^2/2$	0.23	$\varepsilon/2$	$3\varepsilon/4$
Fig. 12	200	3/200	$h/20$	1/200	1/200	$h^2/4$	0.025	–	–	–	–	–
Fig. 13	600	7/300	$h/40$	7/450	–	–	–	7/600	$h^2/2$	0.1	$12\varepsilon/25$	$\varepsilon/2$

perimentally observed effects, such as the formation of double seams, are displayed. Indeed our simulations in Fig. 9, for example, replicate microstructure found in Fe foils exposed to Zn vapour, see [11].

We conclude with a brief comparison of the three models.

- Computations for both the double obstacle phase field and level set method are performed in a narrow transition layer, of width $\pi\varepsilon$ and 2ε, respectively. Across the interfacial layer we found around 15 grid points have been adequate for the purpose of the paper. For small ε the order parameter φ takes the form $\sin(d(\mathbf{x})/\varepsilon)$ across the interface whereas the level set function is approximately $d(\mathbf{x})$ in the neighbourhood of the interface after re-initialization; here $d(\mathbf{x})$ denotes the distance to the zero level set of φ and ω. Observe that for small $d(\cdot)$ the order parameter is close to being a scaled distance function.
- In terms of computation time the sharp interface model is significantly faster than the other two models; however, it has the draw back that topological changes cannot be dealt with.

- The advantage that the phase field model has over the level set model is that no re-initialization procedure is required.

References

[1] J.F. Blowey, C.M. Elliott, Curvature dependent phase boundary motion and parabolic double obstacle problems, in: W.-M. Ni, L.A. Peletier, J.L. Vazquez (Eds.), Degenerate Diffusions, IMA, vol. 47, Springer, New York, 1993, pp. 19–60.
[2] Y-G. Chen, Y. Giga, S. Goto, A stable difference scheme for computing motion of level surfaces by the mean curvature, in: D. Kim et al. (Eds.), Proceedings of the Global Analysis Research Center Symposium, Seoul, Korea, 1994, pp. 1–19.
[3] J.W. Cahn, P. Fife, O. Penrose, A phase field model for diffusion-induced grain-boundary motion, Acta Mater. 45 (1997) 4397–4413.
[4] K. Deckelnick, C.M. Elliott, An existence and uniqueness result for a phase-field model of diffusion-induced grain-boundary motion, Proc. Roy. Soc. Edin. Ser. A. 131 (2001) 1323–1344.
[5] K. Deckelnick, C.M. Elliott, Finite element error bounds for a curve shrinking with prescribed normal contact to a fixed boundary, IMA J. Numer. Anal. 18 (1998) 635–654.
[6] K. Deckelnick, C.M. Elliott, V. Styles, Numerical diffusion induced grain boundary motion, Interfaces Free Boundaries 3 (2001) 393–414.
[7] G. Dziuk, Convergence of a semi-discrete scheme for curve shortening flow, Math. Models Meth. Appl. Sci. 4 (1994) 589–606.
[8] C.M. Elliott, Approximation of curvature dependent motion, in: I. Duff, G.A. Watson (Eds.), State of the Art in Numerical Analysis, Clarendon Press, Oxford, 1997, pp. 407–440.
[9] P. Fife, J.W. Cahn, C.M. Elliott, A free boundary model for diffusion-induced grain-boundary motion, Interfaces Free Boundaries 3 (2001) 291–336.
[10] P. Fife, X.-P. Wang, Chemically induced grain boundary dynamics, forced motion by curvature, and the appearance of double seams, Euro. J. Appl. Math. 13 (2002) 25–52.
[11] C. Handwerker, Diffusion-induced grain boundary migration in thin films, in: D. Gupta, P.S. Ho (Eds.), Diffusion Phenomena in Thin Films and Microelectronic Materials, Noyes Publications, Park Ridge, NJ, 1988, pp. 245–322.
[12] U.F. Mayer, G. Simonett, Classical solutions for diffusion induced grain boundary boundary motion, J. Math. Anal. Appl. 234 (1999) 660–674.
[13] E. Rouy, A. Tourin, A viscosity solutions approach to shape-from-shading, SIAM J. Numer. Anal. 29 (1992) 867–884.
[14] J.A. Sethian, Level set methods and fast marching methods, in: Cambridge Monographs on Applied and Computational Mathematics, vol. 3, Cambridge University Press, Cambridge, 1999.